Available online at www.sciencedirect.com
ScienceDirect
Engineering Structures 29 (2007) 2673–2691
ENGINEERING STRUCTURES
www.elsevier.com/locate/engstruct

Global analysis and constructional aspects in the redesign of bearing elements for a movable storm surge barrier

P. Samyn[a,*], W. Van Paepegem[a], J.S. Leendertz[b], E. Suister[b], L. Van Schepdael[c], J. Degrieck[a], P. De Baets[a]

[a] *Ghent University, Laboratory Soete, Department Mechanical Construction and Production, St. Pietersnieuwstraat 41, B-9000 Gent, Belgium*
[b] *Ministry of Transport, Public Works and Water Management, Directorate-General, Herman Gorterhove 4, NL-2700 AB Zoetermeer, The Netherlands*
[c] *SOLICO B.V., Solutions in Composites, Everdenberg 97, NL-4902 TT Oosterhout, The Netherlands*

Received 2 June 2006; received in revised form 12 January 2007; accepted 15 January 2007
Available online 2 March 2007

Abstract

A flexible protection from flooding of lowlands surrounding harbour areas consists of a movable storm surge barrier, such as the Maeslantkering near Rotterdam. It has a curved steel wall that is connected to a pivot element or ball-joint by steel trusses. A critical point in the construction is the rotating ball-joint that controls the movement of the retaining wall into the river. Due to the high forces transmitted between the convex and concave sliding surfaces originating from the hydraulic storm head, waves and wind, a design with thin films consisting of solid lubricants failed. A solution is found by incorporating reinforced polymer bearing elements that offer good dimensional stability and low friction under dry sliding conditions. In present paper, a study is made of the bearing capacity and sliding behaviour of the modified ball-joint in combination with different loading histories during floating, immersion and retaining actions under a full hydraulic head. Loading of the joint by minimum gravity forces and maximum hydraulic forces perpendicular to the gates is the most critical in this respect. Through the application of an elastic bearing layer, the frictional momentum on the ball-joint is influenced by the stiffness, the thickness and the friction coefficient of the sliding material. The dimensional stability and sliding behaviour of the bearing elements is experimentally investigated by large-scale testing, and it is verified by finite element models that both the polymer elements and the steel structure have sufficient strength to carry the loads while retaining a storm. Their reliability is verified by two on-the-field test operations.

Keywords: Storm surge barrier; Strength; Friction; Loading history; Polymer; Bearing

1. Introduction

Protecting the inlands against a water flood has become an urgent issue, because the human catastrophe and financial costs caused by a storm are enormous. Countries and cities all over the world are threatened by disasters, most recently in New Orleans, America (November 2005). Lands below sea level should be adequately protected, and since the historic flood in The Netherlands in 1953 described by Gerritsen [1], a set of measures were put forward in the Delta Act. Consequences were published by Van Dantzig and Kriens [2]. The province of South Holland is nowadays protected by dams and the elevation of dikes, while a more flexible form of protection is needed near harbours. As the port of Rotterdam is one of the world-leading sea traffic zones and a densely populated area with over one million inhabitants, it should be adequately shielded while providing access to container ships without any height restriction via the "Nieuwe Waterweg".

One solution is found in the construction of a movable storm surge barrier with sector gates. The barrier consists of two hollow hemispherical steel structures swung from the banks into the river and sunk on the river bed. Because the hydraulic head thrust is directed radially towards the vertical rotation axis, the load is almost completely balanced, and the barrier can be opened and closed with a differential hydraulic head across the gate. When the retaining walls are not in operation, both gates are parked in docks on the river banks with the

* Corresponding author. Tel.: +32 9 264 33 08; fax: +32 9 264 32 95.
E-mail address: Pieter.Samyn@UGent.be (P. Samyn).

0141-0296/$ - see front matter
doi:10.1016/j.engstruct.2007.01.012

water level 1 m below ebb tide level. A closing operation, as defined by Vollebregt et al. [3], is initiated when an expected storm level exceeds 3.20 m above datum. After the docks are filled with water, the rotation of the walls is controlled by a ball-joint structure. This floating action takes approximately 1 h. The walls are subsequently immersed to the bottom of the river by filling the ballasting cavities with water. Immersion takes approximately 0.5 h. The in-service time is designed at 30 h, corresponding to a storm with double hydraulic head. The reverse lifting and floating operations take 2 h and 0.5 h respectively.

During the closure of the storm surge barrier, it protects the inland part of the harbour. The seiches occurring in the semi-closed basin of the Rotterdam harbour were analysed by De Jong and Battjes [4]. Seiches occur in the temporary basin of the Nieuwe Waterweg, with a dominant eigenperiod of approximately 30 min. The heights of the seiches were further analysed, as they possibly contribute to the failure probability of the barrier. Under specific circumstances, the trough of a seiche causes a critical situation when the water level on the sea side of the barrier drops below the level on the river side. In extreme situations, it causes failure of the storm surge barrier since it is primarily designed for protection against high water levels on the sea side. If the net seaward force becomes too large, the ball-joint structure possibly disrupts.

Building a flexible barrier of extremely large dimension and weight requires high-tech design, fabrication and assembling standards. A most critical point in the structure is the ball-joint controlling the functionality and movements of the barrier. The barrier was originally commissioned in 1997, but wear marks were observed at the bottom concave bearings and the supporting ring elements after a test operation in 1999. The construction was put out-of-service. This was the impulse for an analysis of the entire construction and re-design of the bearing elements in the ball-joint, considering mechanical, tribological and material science aspects. A multidisciplinary team with the Ministry of Transport, Water Management and Public Works, Civil Engineering Division (Nederlandse Rijkswaterstaat), The Bouwcombinatie Maeslantkering (the original contractor), Solico (Solutions in Composites), Materialprüfungsanstalt der Universität Stuttgart (MPA) and Ghent University was involved in a project to make the structure functional within the period 2000–2003. The project was finished and verified by a test operation of the barrier in September 2004.

The present paper gives an overview of the theoretical analysis made for the global structure and important issues in the practical realisation of the ball-joint. In order to increase its structural reliability, maintenance of the ball-joint should be limited and frictional forces should be overcome by using self-lubricating materials. The novelty in the practical design of the present off-shore construction is that polymer bearing elements are used under extremely high contact pressures, exceeding compressive yield strengths. The continuous bearing layer should be transformed into discrete bearing elements to ensure the dimensional stability of the polymer elements. It is clear that the stiffness, coefficient of friction and thickness of the bearing layer strongly alter the performance of the ball-joint. A problem at present is that coefficients of friction or stiffness for large constructions are often difficult to estimate, because laboratory tests are mostly done on small-scale equipment. It is discussed in this paper how theoretical finite element modelling is used to determine representative large-scale test conditions. The novelty in theoretical issues includes a global analysis of the ball-joint functionality based on different loading histories with static and hydraulic loads on the storm surge barrier. The global analysis is translated into a description of the local behaviour of the polymer sliding elements, which is used for the selection of the material type and geometry. The local behaviour of the bearing elements in the joint is experimentally verified by large-scale tests under static and dynamic conditions and by using a local finite element analysis by Van Schepdael et al. [5]. The present design is unique as it requires ad hoc large-scale testing facilities and a simulation of the in situ behaviour of the bearing elements as close to practice as possible, for verification of the theoretical calculations.

2. Original design of the moveable storm surge barrier

Five international consortia were asked in the summer of 1987 to present a conceptual design for the realization of the barrier. The final selection in 1989 was made in favour of the BMK Barrier Design and Construction Group. The principal parts of the Maeslant storm surge barrier are presented in Fig. 1(a). It has an identical structure on the North and South river banks with a span of 360 m, consisting of a sill and river bed protection; a retaining wall with length 210 m, height 22 m, width of 15 m and steel weight of 7000 ton; tubular space trusses of 250 m length and steel weight of 7000 ton; a pivot element or ball-joint with diameter 10 m and weight of 680 ton. The horizontal gate movements are generated by an engine with electrical pumps and hydro-engines with a capacity of 1500 kN. The works in the river, e.g. the support of the barrier on fenders and the river bed protection, were reviewed by Vanoorschot and Pruijssers [6].

2.1. Description

- The *retaining wall* (Fig. 1(b)) consists of an orthotropic plate structure similar to a curved ship's hull. It is made of plate structures stiffened with triangular sections, having a minimum of welds and a small surface area to paint. The lower part contains inlet valves and pumps for ballasting and deballasting. The upper part is a passive tank. The front wall retains the waves, and the wall at the riverside withstands the hydraulic head during operation. During the "in service" period, the retaining wall is supported by fenders in sleighs that move over the sill blocks. During the "out of service" period, the retaining wall is supported by elastomeric bearings.
- The *tubular steel trusses* (Fig. 1(c)) have one top chord and two bottom chords. The distance between the top chord and the plane of the bottom chords is 18 m. The distance between two bottom chords is 15 m. A triangular truss section is made from two inclined vertical trusses connecting

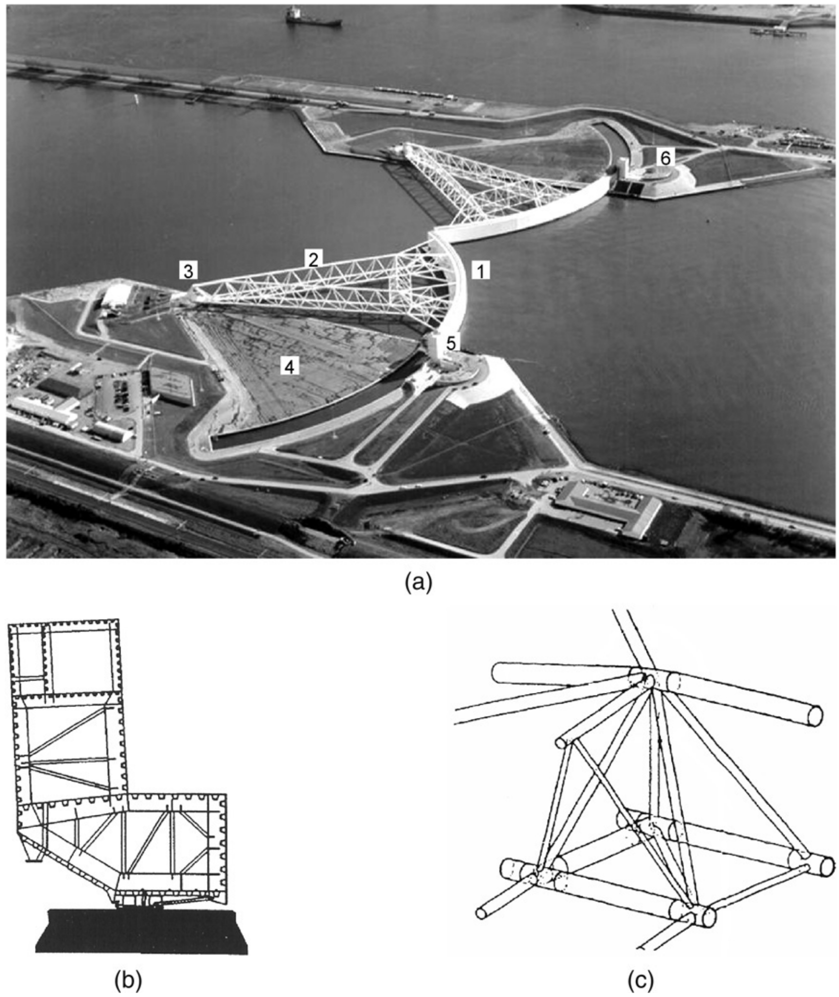

Fig. 1. Principal parts of the Maeslant storm surge barrier, (a) general overview: (1) retaining wall, (2) triangular space trusses, (3) ball-joint, (4) parking dock, (5) control engines, (6) control centre; (b) detail of the retaining wall; (c) detail of the steel trusses.

the horizontal bottom chords with a common top chord. The trusses contain no diagonals, thus avoiding secondary effects related to any contraction of the chords. The top and bottom chords have a diameter of 1800 m and wall thickness from 45 to 90 mm. Every tube is manufactured from rolled plates of length 4 m. These parts are assembled on-site into complete tubes with discontinuous seams. The diagonals have a diameter of 800 mm and a wall thickness of 16 mm. They are manufactured from strips through a spiral rolling and welding process. The spreader elements are connected by another space truss. The transverse coupling truss acts as a bottom chord in a system where the retaining wall acts as a top chord. The BMK design team found out that the available material and welding specifications could not be used for this construction due to high strength requirements, large thickness, assembling and welding connections, etc. Material specifications are detailed by Zondervan [7].

- A *connection element* is designed where both trusses come together near the ball-joint. For stability reasons, circular sections are transferred into square sections with a cast steel element. The truss joint is detailed with two plates forming a flexible connection in the longitudinal direction and a rigid connection in the transverse direction between the chords. Force concentrations are avoided as such. The rectangular sections couple the top and bottom space trusses together and connect them to the rectangular box sections of the ball-joint kernel.
- The *ball-joint* in the abutments of the construction is detailed in Fig. 2. The kernel has a rectangular box structure with four webs connected to the steel trusses. The shape of the faceted ball-joint is achieved by convex elements bolted to the kernel. The front and back bearings consist of convex cast steel scales (St 52.3) in contact with a concave chair structure of cast iron. The bottom bearing contains a convex ring structure with eight concave supports. With a tolerance on the convex and concave parts of ± 1.0 mm, the convex parts have a diameter of 10.0 m and the concave parts have a diameter of 10.04 m, or $\Delta R = 20$ mm. Rotations of the walls and deformations of the structure cause the ball to slide over the bottom and back chairs, transmitting respectively vertical and horizontal loads to the anchor block. Forces are introduced into the foundation that acts as a gravity structure. During the "out of service" period, the ball joint is supported by coupled hydraulic jacks that are permanently under pressure to avoid damage to the contact surfaces by fretting. The convex parts can be lifted over 500 mm for

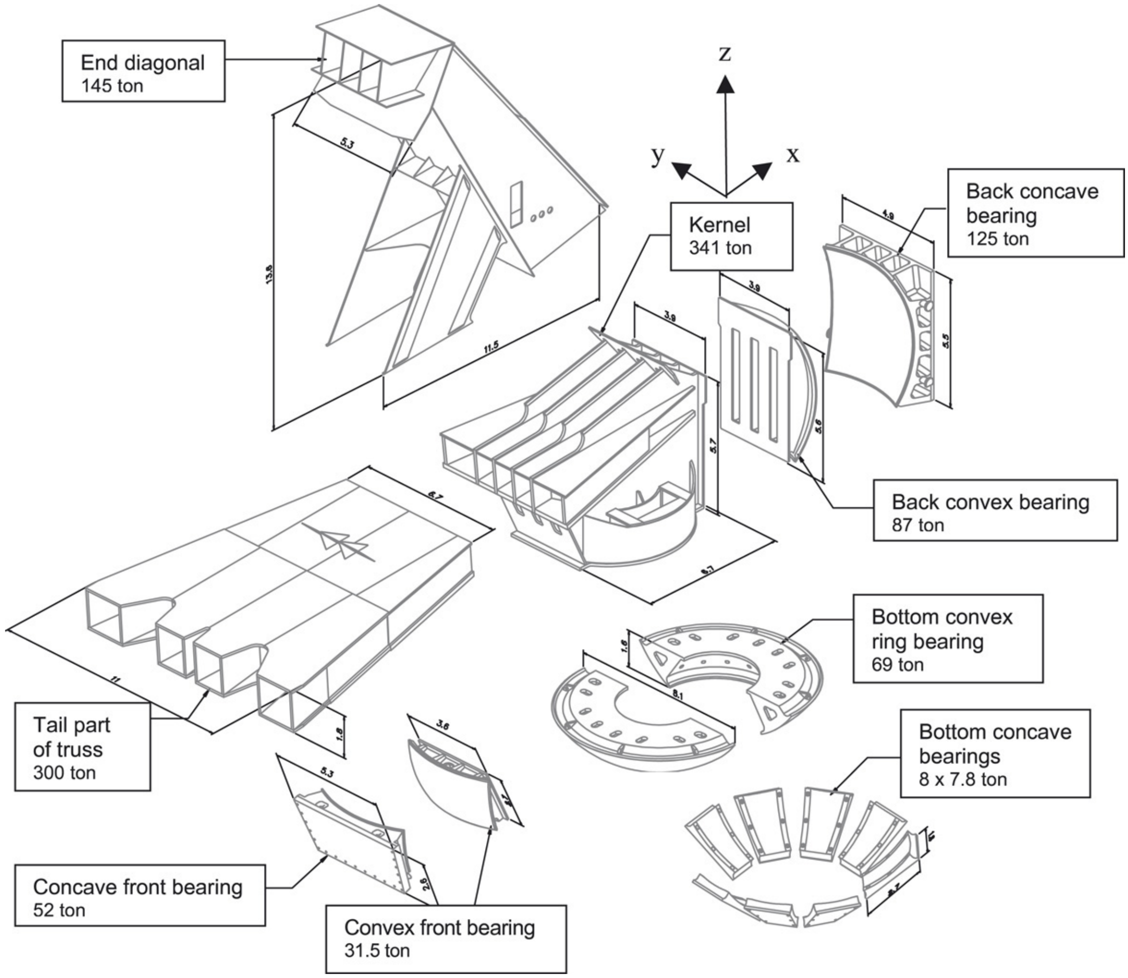

Fig. 2. Detail of the ball-joint construction.

inspection and maintenance. The ball-joint is surrounded by a climate conditioned room at 60% constant relative humidity and 23 °C constant environmental temperature.

2.2. Functioning characteristics

The ball-joint rotates at 0.033 rad/min during operation, describing a complex motion according to the orthogonal axis introduced in Fig. 2. It has a maximum floating angle $\varphi_Z = +1$ rad (57°), an angle $\varphi_Y = -0.05$ to $+0.013$ rad ($-2.86°$ to $+0.72°$) during immersion and lifting and a maximum variation $\varphi_X = -0.01$ to $+0.01$ rad ($-0.61°$ to $+0.61°$) through the action of wind and waves.

The load transfer between the convex and concave surfaces of the ball-joint is shown in Fig. 3. The evolution from pure gravity loads (trusses + ball-joint) towards the full positive hydraulic head is illustrated. The positions and the magnitudes of the transmitted load are indicated by contact spots. The forces acting on the sliding surfaces for every operation phase are calculated from a loading history (Fig. 4). The load during floating is introduced through the bottom bearing, with a vertical force resulting from gravity forces of the steel trusses and the ball-joint structure. The maximum design vertical load is $F_z = 42 \cdot 10^6$ N. It balances the tensile and compressive forces as well as transverse forces implied by the wind and waves, so that the bearing is not disrupted from its position. After immersion, the retaining wall is supported by sill blocks and through the tilted position of the trusses, the vertical reaction force lowers to a minimum design value $F_z = 27 \cdot 10^6$ N. The resultant bearing force turns into a more horizontal direction and attains a value of $275 \cdot 10^6$ N under a full positive hydraulic head (compressive load from sea side onto the bearing, 6.5 m). The additional effects of waves (with initial height approximately 2.5 m and amplification through reflection) count for a resulting force $4 \cdot 10^6$ N; wind forces are $6.5 \cdot 10^6$ N (mainly F_y) and water currents during floatation amount to $15 \cdot 10^6$ N. The design value for the resultant bearing force is then $F_x = 350 \cdot 10^6$ N. This load is carried by the back bearing. A situation with a negative hydraulic head (high water level at the riverside causing tensile forces on the bearing, 1.5 m) possibly occurs after a storm, with a horizontal force $F_x = -50 \cdot 10^6$ N acting on the front bearing.

The trusses are designed to transmit the loads from the retaining wall to the pivot element. The entire load under a full positive hydraulic head is mainly taken by the chords in the bottom plane. The top chords and diagonals mainly carry the

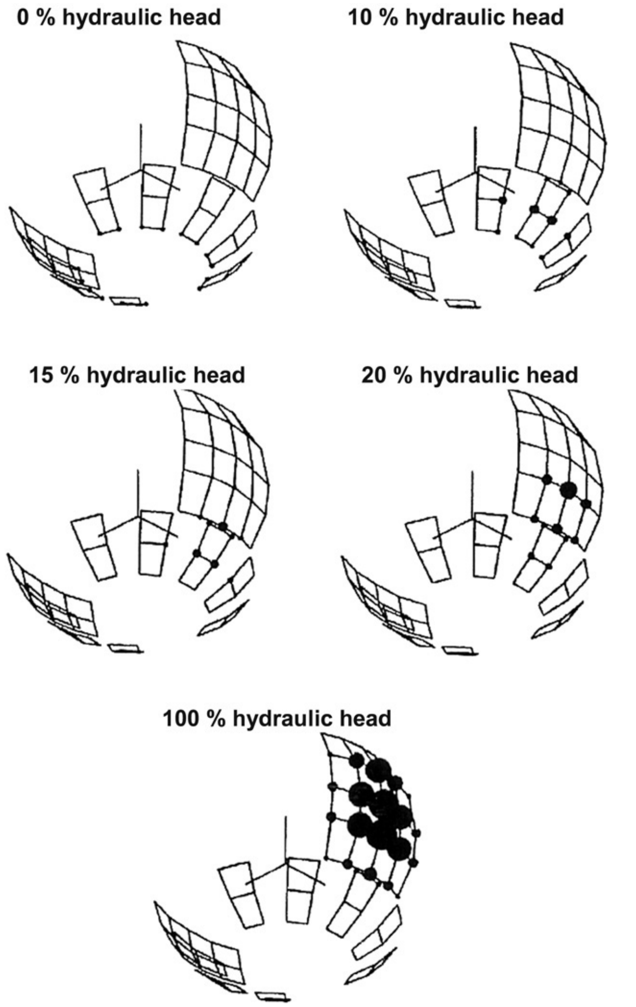

Fig. 3. Load transfer between convex and concave bearing parts between pure gravity forces and the full hydraulic head.

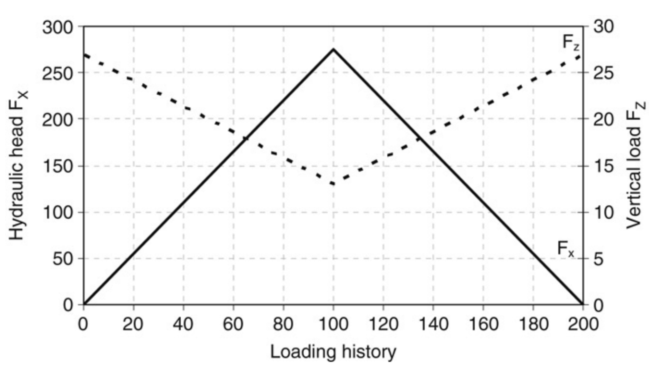

Fig. 4. Vertical load F_z (gravity weight) and horizontal load F_x (hydraulic head) on the bearing elements.

dead weight and work as stabilizers. The transverse coupling truss does not act as a main load carrying element. It reduces the horizontal bending effects caused by waves and wind, limiting fatigue problems. The bottom chords near the ball-joint are somewhat lifted in order to direct the resultant horizontal compressive forces in a straight line to the back bearing.

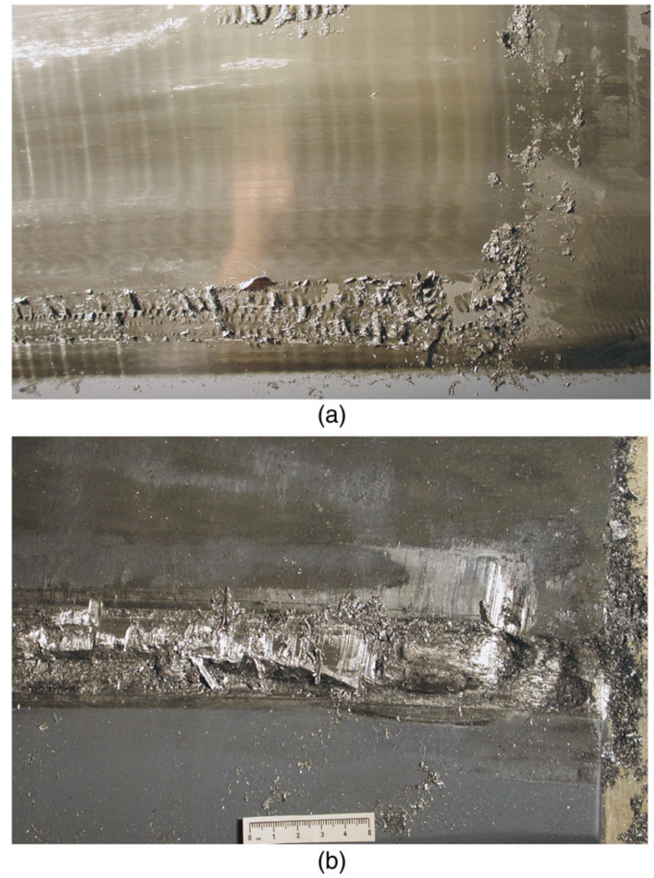

Fig. 5. Failure of thin lubricant film on the sliding surfaces of the original ball-joint, (a) delamination of MoS_2 spray, (b) cold welding spots on bottom bearing elements.

3. Ball-joint failure and design modification

3.1. Thin film lubrication

In the original concept (1987), friction and load transfer between bearing surfaces was planned to be overcome by covering the convex surfaces (cast steel) with an asbestos-containing polymer and an aluminum bronze coating on the concave surfaces (cast iron). It provides a coefficient of friction $\mu = 0.30$ and a relatively low reaction momentum compared to an unlubricated cast steel/cast iron contact ($\mu = 0.60$). The supporting concrete structures have low stiffness and could not meet the tolerances. Also for ecological reasons, alternatives were investigated, resulting in the application of a 10 μm thick layer on the sliding surfaces, being a mixture of resin with MoS_2 lubricant (1997). For running-in purposes an additional layer of PTFE-spray was applied to lower the initial static friction. The duplex coating system has a final thickness of 20–40 μm, with a design coefficient of friction $\mu = 0.15$. It functions under controlled climate conditions.

Wear marks were observed on the bearing elements after a test operation (1999), including loss of the MoS_2 coating on the ball surface and cold welding spots between the convex and the concave surfaces (Fig. 5). In the following years, similar damage was observed. The wear did not immediately threaten the functionality and strength of the barrier, but it caused many

Table 1
Design requirements for the alternative bearing concept

	Design aspect	Requirement
1	Global behaviour	Modification of the difference in radii ΔR between the convex and concave parts shall not affect substantially the resultant bearing force and its position.
2	Strength of steel structures	The strength of the existing trusses and the steel structure of the ball-joint shall not be exceeded for transfer of loads between convex and concave surfaces.
3	Clearance	Sufficient space between the convex rear bearing and concave rear bearing during floating out should be verified for lower ΔR.
4	Friction coefficient	Global values of 0.15 should be increased to 0.25 with control of the frictional moment. The effect of a locally higher friction coefficient should be verified.
5	Wear	Total wear path of 300 m over 5 years is required, being the slide path for the worst location.
6	Post-critical behaviour	The deformation due to elastic and plastic compression and the loss of material due to wear shall not lead to any contact between the convex and the concave parts.
7	Durability and maintenance	The minimum requirement is related to the functioning over 1 year without maintenance of the structural elements; the life-time of the full construction is 100 years.
8	Environment	The materials shall not be in conflict with the environmental laws.
9	Manufacturing and erection	In situ modification of the ball-joint within 4 months.
10	Research and development	No time is available for fundamental research on coating technology, only further development of known materials and techniques can be applied.

repair works and out-of-service periods. Successive repairs progressively degraded the surfaces. Although a 10 years life-time for the thin film was assumed, an analysis of the wear leads to the following conclusions:

- Intermediate test operations of the barrier were not considered as an original design criterion. Due to more frequent use, the surfaces of the concave bearings in the bottom were increasingly stressed.
- The small-scale specimens used for qualification tests on the laboratory scale caused lower edge stresses than in the real construction. Small-scale tests were not representative for the real construction.
- The quality of the sprayed MoS_2 layer showed a fluctuating quality.

3.2. Alternative bearing concept

The development of new sliding coatings with thickness 200–300 μm is impossible within the present technical boundary conditions and short time limits. Alternative concepts for a boundary layer between the concave and convex surfaces are suggested, according to the design requirements in Table 1. Meanwhile, the design life-time should be increased to 100 years, and the ball-joint should function without additional maintenance during one year, including one testing operation and one storm surge with two successive hydraulic tops. The total sliding distance of the ball-joint is therefore increased to 300 m.

The proposed final bearing concept consists of a hard counterface in contact with a relatively soft sliding material, and offers possibilities for eventual lubrication during running-in. Different material combinations are put forward and a first selection is based on application methods, friction and loading capacity:

- The convex part is a continuous surface and it should have high hardness and wear resistance, while it should be protected against corrosion. Bare cast steel is therefore not an option. Two-component coatings, ceramic coatings and metallic coatings (e.g. stainless steel, TiN, Al) are considered, but they are unsuitable for in situ application within a small space between the sliding surfaces. Moreover, the original steel roughness $Ra = 3.2$ μm does not ensure good adhesion. The use of a MoS_2 spray coating is impossible through low adhesion at the given roughness. Coating degradation through ageing and contact with water will cause severe wear. A zinc–phosphate primer coating is a better option, with good adhesion at given roughness. Its friction and wear behaviour depending on the application method and ageing time, will be further investigated.
- The concave surfaces should contain a relatively soft and flexible material with high load-carrying capacity, wear resistance and low creep. Sheets can be featured over the concave parts, but they are unable to transfer the friction forces parallel to the surface into the concave bearings. Different constrained polymer and composite materials are selected, e.g. polyamide (PA), teflon (PTFE), polyester/polyester composites and ultra high molecular weight polyethylene (UHMWPE). However, polyamides are unfavourable because of stick-slip effects in dry sliding (Van de Velde and De Baets [8]) and the loading capacity of teflon for present application is intolerable (Blanchet and Kennedy [9]).

3.3. Polymer bearing pads

A first design of 'free' polyester/polyester composite pads bolted on the concave surfaces is considered. Forces are transmitted from the convex onto the concave surface and foundation of the structure, through friction between the composite bottom surface and the concave steel surface. The friction between the composite top surface and the convex cast steel should be lower than the friction between the composite bottom surface and the concave cast iron. This is made possible by introducing a solid lubricant on the top sliding surface and increasing the roughness of the bottom sliding surface. A polymer screw in the centre of the pad is used for axial fixation, while the permanent positioning of the pads is ensured by a high coefficient of friction between the composite pad and the concave surface. The elasticity of 'free' polymer pads is favourable for local deformation and insensitive to manufacturing tolerances. However, a large deformation of the top lubricated layer and catastrophic wear of the primer coating on the convex surface were experienced during sliding experiments.

The final design has 468 constrained hybrid UHMWPE pads incorporated into holes machined on the concave back, bottom and front chairs of the ball-joint. A detail of a single pad is shown in Fig. 6. The pad has a nominal diameter of 249.50 mm and a thickness of 40 mm, while the holes have a diameter of 250 mm and a depth of 32 mm. The polymer has a free surface of 8 mm above the concave chair structures, and is in contact with the convex steel counterface. The pad is therefore dimensionally stabilised with a carbon fibre reinforcing ring. A polymer lip protects against direct contact between the convex steel and the carbon ring, leading to unacceptable wear. Holes on the sliding surface possibly contain lubricant, although low friction under dry sliding conditions will be demonstrated. In contrast to 'free' bearing elements, two elements need further analysis: (i) the tolerances on the diameter and the thickness of polymer pads and machined holes determine local deformation and stiffness, and (ii) forces between the convex and concave surfaces will be transferred through the walls of the machined holes, and the strength of the remaining steel structure should be verified.

4. Global analysis of the modified ball-joint

The effects of an elastic layer between the concave and convex sliding surfaces of the ball-joint are discussed in relation to the strength and behaviour of the entire steel structure. In a first approach, the bearing layer is considered as a continuous elastic layer. In a second step, the distribution of the discrete polymer bearing pads is discussed to determine the local contact pressures for every pad.

4.1. Continuous elastic layer with full bearing area

The influence of the bearing layer's thickness and stiffness on the contact pressures in the ball-joint is investigated with a non-linear time history analysis. The effect of various coefficients of friction on the sliding behaviour is verified with a two dimensional simulation. As the polymer sliding surfaces are 8 mm above the concave steel surfaces, the difference in radii ΔR between the convex and concave surfaces decreases from 20 to 12 mm and is possibly further influenced by creep (calculations for $\Delta R = 10$ mm are representative for the 8 mm free surface, taking deformation into account). The properties of the elastic interlayer and its lower thickness stability compared to the infinitely stiff MoS_2 coating influence the global sliding behaviour of the convex/concave sliding couple (rolling, slip, position of resultant force) and the local behaviour (contact area and maximum contact pressure).

(a) *Effect of layer thickness and stiffness*

The contact pressures over the elastic interlayer cannot be calculated from the Hertz theory, as it considers an infinitely small and continuous bearing surface in contrast to the faceted ball-joint. The load distribution over the bearing surfaces is therefore modelled in agreement with the geometry and stiffness of every concave structure. Local variations in the stiffness of the concave structures due to supports or changes in cross section are not considered. Corrections will be made during the implementation of the local contact pressure distribution for every bearing element. Contact elements of approximately 1 m^2 are used, transmitting radial and frictional forces. The transverse contraction of the elastic layer is not taken into account. Stress concentrations are expected near the edges of the bearing surfaces and are important for running-in. Contact elements at the borders are therefore refined to 0.5 m^2. The contact stresses on the back, front and bottom concave bearings are calculated for different loading histories, including (i) the original gravity weight, (ii) floating, (iii) retaining a 100% hydraulic head (waves perpendicular to the sector gates) and (iv) a negative hydraulic head. The vertical reaction force on the ball-joint originates from gravity weight of the sector gates and is corrected with an additional factor depending on parked, floating or retaining positions. Loading the joint with minimum gravity forces and maximum hydraulic forces perpendicular to the gates is the most critical.

Contact stresses are calculated for every contact element on the concave surfaces, and are illustrated in Fig. 7 for $\Delta R = 5$ mm, $E = 1000$ MPa, $\mu = 0.15$. It shows a maximum load either on the back bearing (during retaining) or on the bottom bearing (during floating). The maximum contact stresses on the bearing interlayer are summarised in Table 2. Variable thickness $d = 19, 15, 10$ mm (respectively $\Delta R = 1, 5, 10$ mm), variable elasticity $E = 100, 1000$ and $10\,000$ MPa and a hypothetic coefficient of friction $\mu = 0.15$ or 0.25 are used. The present simulations consider 100% bearing area and will be further corrected.

It is concluded that only the bottom bearing variations in ΔR and E hugely change the contact pressures, while variations in elasticity between 1000 and 10 000 MPa almost do not influence the contact conditions. Contact pressures on the front chair are inferior and are not further considered. Calculations with higher coefficients of friction indicate only a slight variation in contact stresses, while the global strength of the structure is not exceeded. Specifically during floating, when

Table 2
Global FEM analysis for contact pressure on the elastic bearing interlayer with variations in thickness, friction and elasticity

Loading history		First sliding stroke	Steady-state sliding						Total available bearing area (m^2)
Elasticity-modulus (MPa)		10^3–10^4	10^2	10^3				10^4	
ΔR (mm)		10	5	1	5	10		5	
Coefficient of friction (−)		0.25	0.15	0.15	0.15	0.15	0.25	0.15	
	Back-chair	7	36	36	34	32	31	34	22.67
Contact pressure (MPa)	Bottom-chair	18	23	25	32	33	34	31	2.08
	Front-chair	5	22	21	22	20	21	20	10.62

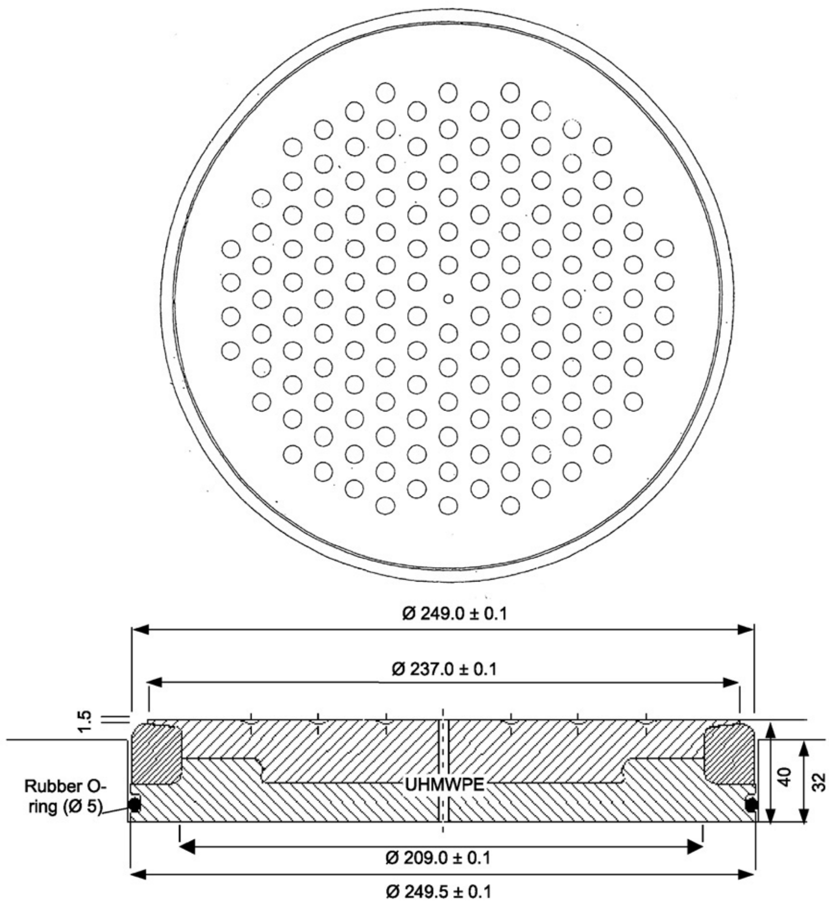

Fig. 6. Hybrid UHMWPE pads with carbon fibre/epoxy rings constrained in machined holes.

only the bottom bearing is loaded, high coefficients of friction (up to 0.50) do not exceed the constructional strength, as the full bearing capacity is not yet used. Also for the first sliding movement on the back and bottom bearing, higher friction is tolerated when the loads and contact pressures are low. A maximum coefficient of friction of 0.25 is allowed for all other loading histories at $\Delta R = 10$ mm. The case of $\Delta R = 10$ mm is an optimum: a higher ΔR causes an increase in contact pressures and a lower ΔR possibly results in direct contact between the scales and chairs during sliding, estimated from dimensional imperfections. The case of $\Delta R = 1$ mm is only theoretically considered, as it is practically too small for smooth sliding between the convex and concave surfaces at running-in.

A reduction of ΔR implies a smaller space between the sliding surfaces, causing contact during floating. For $\Delta R = 10$ mm, the theoretical free space is 3.5 mm and it further reduces to 3 mm through negative deformation of the convex surfaces and the manufacturing tolerances of polymer pads and machined holes. For $\Delta R = 5$ mm, the estimated free space equals 1 mm. Under the gravity load of the structure, $\Delta R = 10$ mm provides enough free space between the convex and concave parts. Eventual contact under additional loads from wind and water occurs at low contact pressures. Sliding instabilities or coating removal during floating should be avoided, and both scales are therefore in-situ, modified by a fillet on the running-in edges, and allowing a progressive build-up of

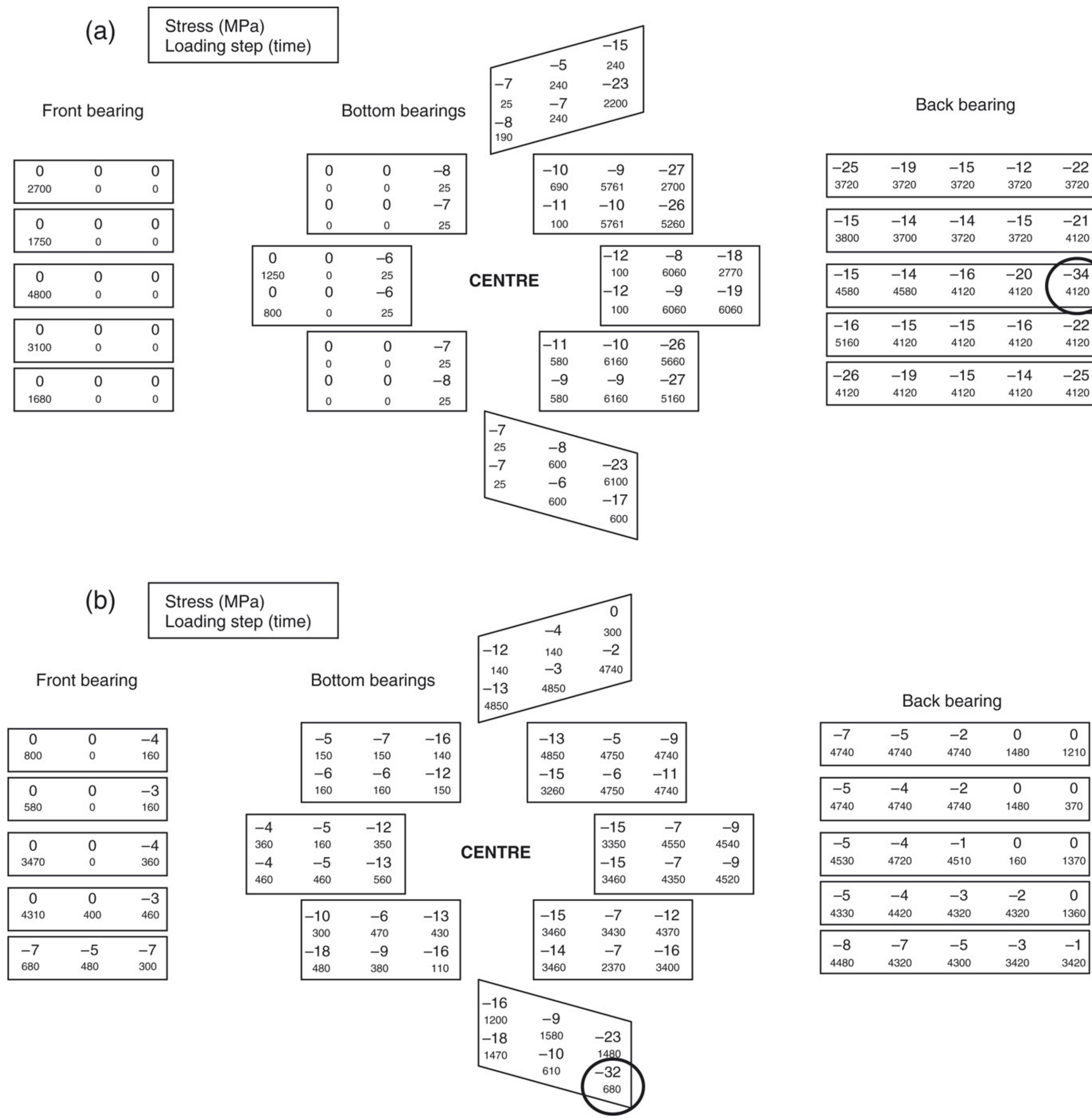

Fig. 7. Illustration of the load distribution over contact elements on the bearing surfaces of the ball-joint for two loading histories: (a) retaining, characteristic for maximum load on back bearing, (b) floating, characteristic for maximum load on bottom bearing.

the contact pressures over the bearing layer. Contacts between the sliding surfaces and asymmetric contact stress distributions over a polymer pad are experimentally verified.

(b) *Effect of friction*

During the rotation of a convex into a concave surface under normal load and zero friction ($\mu = 0$), only slip occurs: there is a parallel translation of the resultant force towards a new centre point while the force direction remains similar. In the case of friction ($\mu > 0$), a combination of rolling and slip occurs: the resultant force direction becomes variable and the relative position between convex and concave changes through the rolling action of the convex relatively to the concave structures. The rolling behaviour is limited when exceeding the maximum frictional force, causing a transition into slip again. The evolution of the bearing force over the concave surfaces for a complete loading history with $\Delta R = 20$ mm is illustrated in Fig. 8, with a coefficient of friction $\mu = 0$ and $\mu = 0.15$. It is concluded that besides the contact stress and magnitude of the bearing force, also its position on the bearing surface is significantly influenced by friction. Small centre point displacements during sliding of the convex surface can be tolerated for $\Delta R = 10$ mm when running-in fillets are applied.

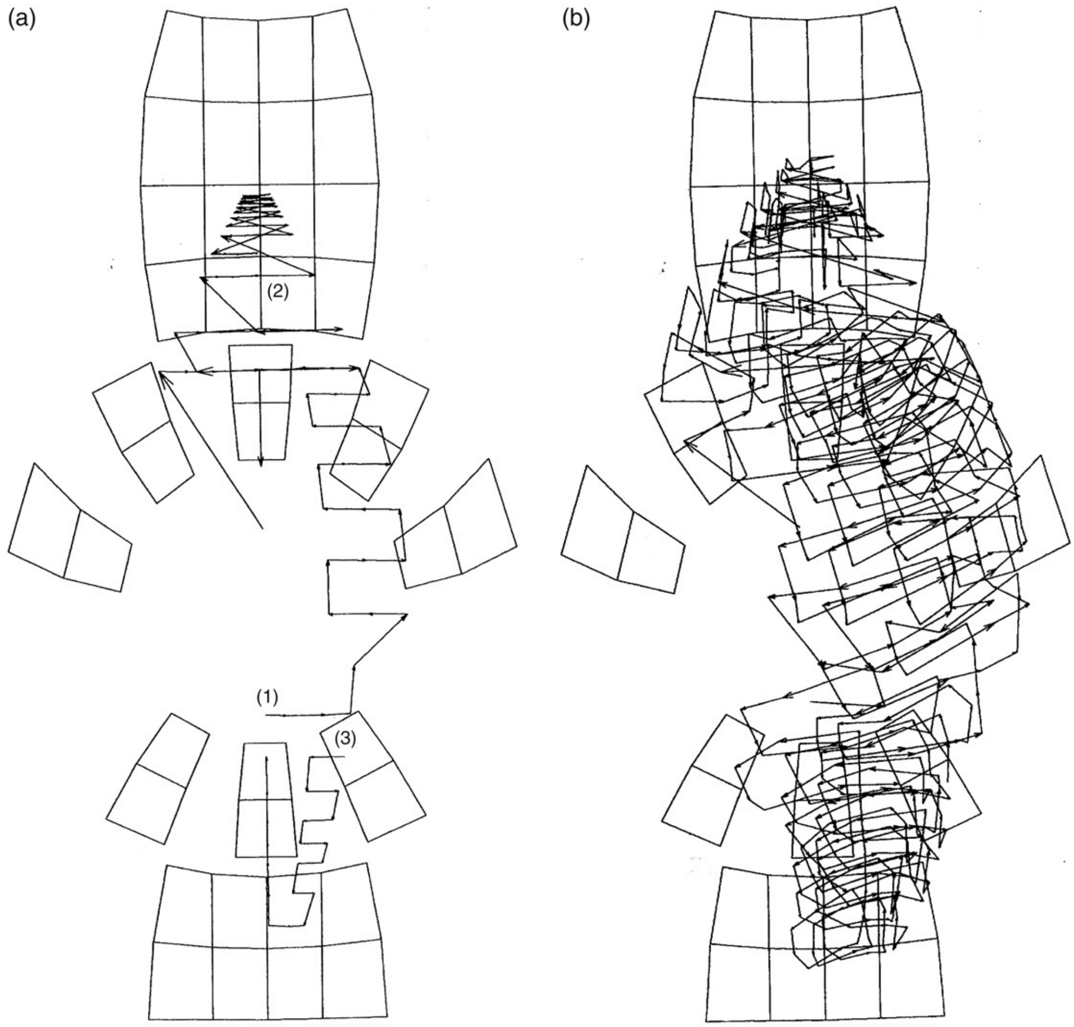

Fig. 8. Variation in position of the resultant bearing force for various friction coefficients of the elastic bearing interlayer, (a) $\mu = 0.0$, (b) $\mu = 0.15$, represented for three loading histories: (1) floating, (2) submersion and retaining, (3) negative hydraulic head.

The eccentricity of the bearing force causes a frictional momentum on the ball-joint. This momentum depends on ΔR and attains a critical maximum value more rapidly for small ΔR values. Therefore, the ball-joint reacts more sensitively on rotations and it is more 'nervous'. For severe rotations of the convex surface into the concave surface, the resultant force attains extreme positions more frequently and some constructional elements are highly loaded in the modified compared to the original design. With a maximum coefficient of friction 0.25 and $\Delta R = 10$ mm, the resultant force on the bearing remains within the constructional strength.

The evolution of the frictional momentum on the ball-joint is calculated in Fig. 9(a). One loading history from the original gravity weight towards a 100% hydraulic head with $\Delta R = 20$ mm, $\mu = 0.15$ is illustrated. A simplified 2-D analysis is used, and it is later confirmed by a 4-D analysis. The direction of the frictional moment reverses during loading as the ball makes an additional rotation φ_y through the deflection of the steel trusses (Fig. 9(b)). The latter represents an elastic upwards bending of the trusses of about 40 mm during hydraulic loading, corresponding to additional rotations of the ball joint over $\varphi_y = 0.0025$ rad (0.14°) per $100 \cdot 10^6$ N hydraulic head. The eccentricity and rotation angle of the resultant bearing force are shown in Fig. 9(c).

The radial reaction forces on the convex surfaces (originating from the concave structures) possibly exceed the bearing force (originating from the retaining wall). The convex surfaces then stick gradually into the concave supports, a phenomenon known as seizure. The maximum momentum on the ball-joint therefore increases and exceeds the theoretical frictional momentum. The effect of seizure is simulated over a full loading history for $\Delta R = 20$ mm (Fig. 10). For a small ΔR and low interlayer stiffness, seizure becomes more important and the maximum momentum on the ball-joint increases by 10% for $\Delta R = 1$ mm. The frictional momentum is critical near the connections between the ball-joint and steel trusses and the structure's strength is verified.

4.2. *Discrete elastic layer of polymer bearing pads*

The theoretical distribution of the polymer bearing elements over the concave chair structures is evaluated in order to optimise the pad geometry (pad diameter and thickness) and to

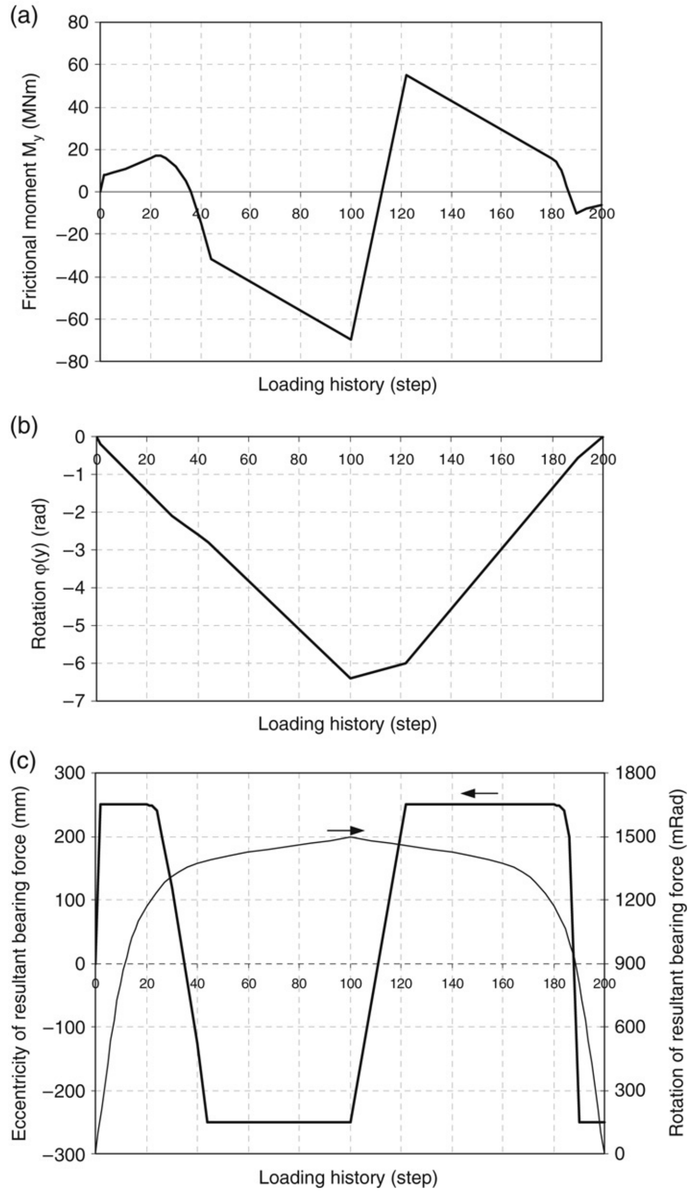

Fig. 9. Analysis of friction, motion and resultant bearing force, (a) frictional moment, (b) rotation of the convex surface, (c) eccentricity and rotation of the resultant bearing force.

minimise the contact stresses on every single element. All pads should have identical diameters from the manufacturing point of view, although patterns with variable pad diameters achieve denser distribution factors. The remaining strength of the steel structure after machining the holes should be verified.

(a) *Distribution of the polymer bearing pads*

The distribution of the pads according to either an orthogonal pattern (90°) or a triangular pattern (60°) is calculated. For every pattern, the theoretical distribution factor is given as a function of the pad diameter in Fig. 11, with an intermediate distance of 50 or 60 mm between two adjacent pads. A theoretical distribution factor of 51% for an orthogonal pattern or 59% for a triangular pattern is attained, with an optimum pad diameter of 250 mm and intermediate distance of 60 mm. Pads with larger diameters do not significantly increase the distribution factor and imply practical concerns, while smaller pad diameters reduce significantly the distribution factor and imply more pads and more holes to be machined. Also for contacts between a convex steel surface and a flat polymer pad, the indentation in the centre of the pad is large compared to the borders when pad diameters increase. This is the origin of uneven load distributions over the pad.

The theoretical distribution factor is translated into effective distribution factors, taking into account the physical geometry and properties of every bearing surface. The selection of a 250 mm pad diameter is mainly based on the optimum distribution over the bottom bearings, as their area is smaller compared to the front and back bearings. The theoretical pattern calculated in a plane, is projected onto the concave surfaces and optimisation is done in respect to the chair structures, considering that: (i) all horizontal sliding paths should be well covered by pads, and (ii) high contact stresses near the borders

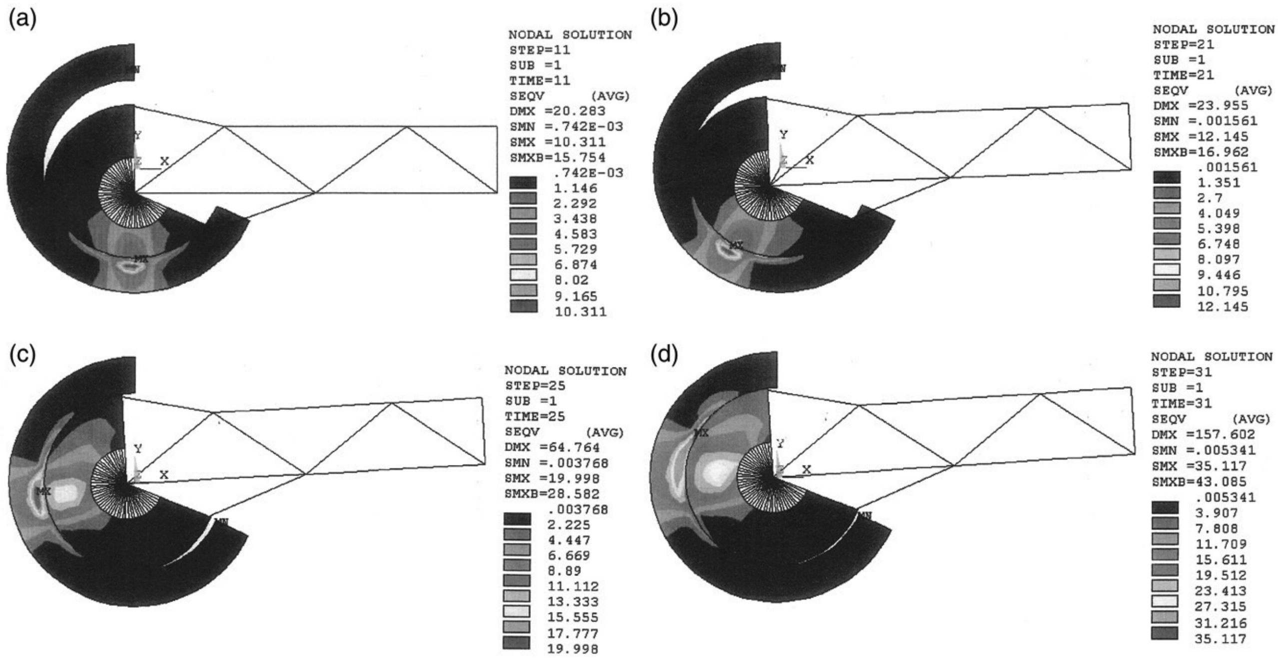

Fig. 10. Frictional moment (MN m) on the bearing (top view) and illustration of the seizing effect for original construction with $\Delta R = 20$ mm, $\mu = 0.15$, (a) pure gravity weight, (b) 10% hydraulic head, (c) 40% hydraulic head, (d) 100% hydraulic head.

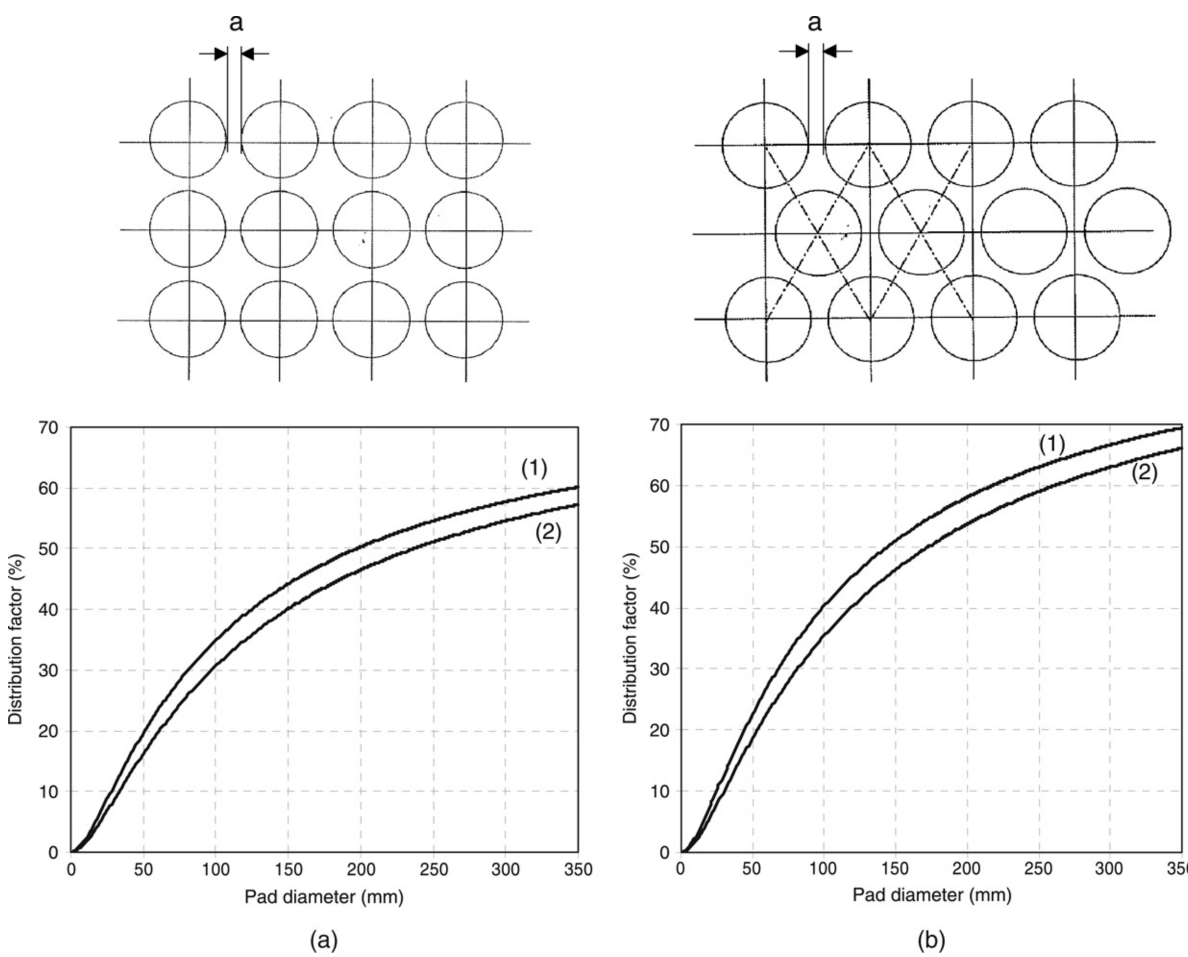

Fig. 11. Theoretical distribution factors for polymer bearing elements for either (a) an orthogonal pattern (curve (1): $a = 50$ mm, curve (2): $a = 60$ mm), (b) a triangular pattern with intermediate distance (curve (1): $a = 50$ mm, curve (2): $a = 60$ mm).

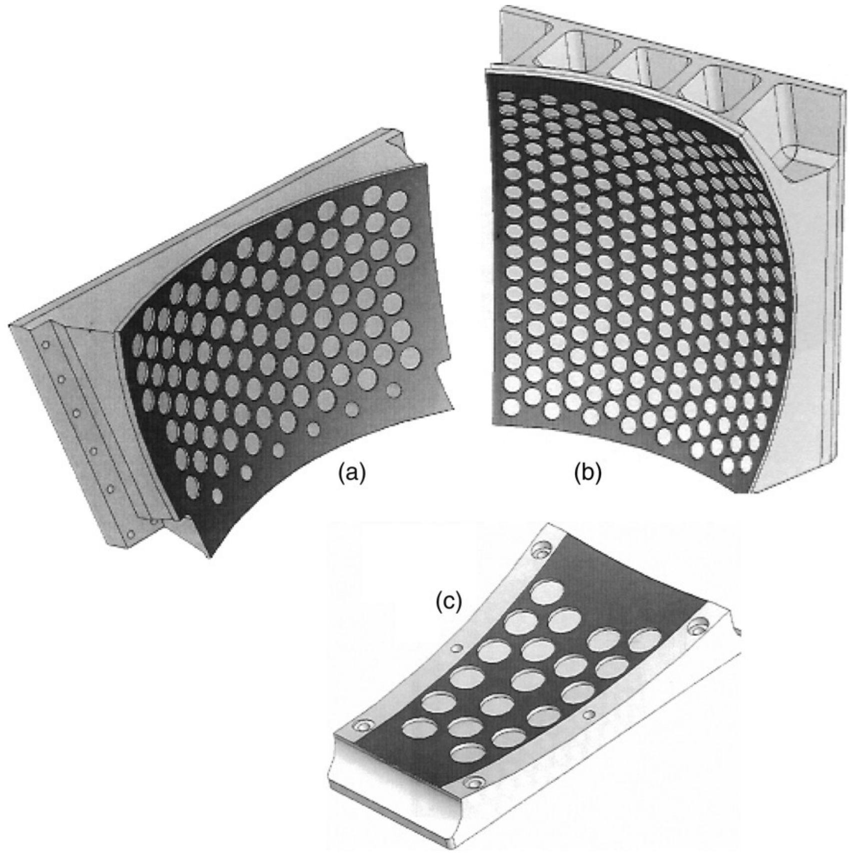

Fig. 12. Practical distribution of polymer bearing elements: (a) front bearing, (b) back bearing, (c) bottom bearing.

require additional pads (Fig. 7). The final pad positions on the back, the front and the bottom convexes are illustrated in Fig. 12, resulting in an effective distribution factor (or bearing area) of 43.8% (bottom), 45.8% (back) and 41% (front). Every bottom bearing has 19 pads, the back bearing has 217 pads and the front bearing has 91 pads.

(b) *Dimensioning and tolerances of polymer bearing pads*

The ball-joint functionality depends on the clearance between the convex and concave surfaces. The height position of the polymer pads determines an "average bearing surface". Variations in height result from deformation, indirectly controlled by the stiffness of the individual pads.

The tolerances on the thickness of the elastic interlayer are evaluated in Table 3. The tolerances on the concave and convex bearing surfaces are statistically determined using a 95% confidence limit. Combined with the tolerances on the polymer pad, the variation on the thickness of the elastic interlayer can be calculated.

- Tolerances on the convex and concave steel structures are determined by on-the-field measurements, resulting in ± 0.18 and ± 0.15 mm tolerances for the back-chair and back-scale respectively (95% confidence limit), which are acceptable from a steel casting process. For this reason, the physical centre of the bearing surface is not at the origin (0, 0, 0) but it is shifted towards (-0.04, -0.18, -0.18), with reorientation of the resultant bearing force (Section 4.1).
- Tolerances on the machined holes are ± 0.2 mm, according to the manufacturing process.
- Tolerances on the polymer pads are ± 0.2 mm, taking into account mould shrinkage and thermal expansion: the polymer pads are moulded and cooled to -20 °C for mounting the carbon fibre/epoxy ring.

Analysis of the back-scale structure shows that respectively 11 pads (95% confidence limit) or 2 pads (99% confidence limit) have smaller or larger dimensions. For the bottom-scale structure, the tolerances are exceeded for 8 pads (95% confidence limit) or 1 pad (99% confidence limit).

The thickness variation of the elastic interlayer causes visco-elastic indentation of the polymer pads, leading to additional stresses on individual pads. The tolerances are converted into values used to calculate the stress distribution with a safety factor 1.50: The maximum variation ± 0.56 mm on the radial position of the back bearing surface and the maximum variation ± 0.72 mm on the radial position of the bottom bearing surface are implemented as additional indentations on a single polymer pad.

It is concluded that the tolerance on the position of the bearing surfaces is strongly influenced by the local tolerances of individual pad and hole dimensions rather than by the global inaccuracy of the convex and concave surfaces. From experimental testing (Section 5), the tolerances on pad diameters are 249.5 ± 0.1 mm and the tolerances on hole diameters are 250 ± 0.25 mm. The tolerances on the carbon fibre/epoxy reinforcing ring are 248.5 ± 0.1 mm. If necessary, the diameter of the machined hole should be increased by 1 mm within the required tolerances. An oversized hole should then

Table 3
Dimensioning of the hybrid UHMWPE pads and machined holes with tolerances for the final bearing layer on the back and bottom bearings (the front bearing is inferior)

Component	Radial tolerance of bearing (mm)	Calculation value for stress verification (safety factor)
Depth machined holes	±0.20	
Thickness hybrid UHMPWE pad	±0.20	
Combination hole/pad	±0.28	
Back chair	±0.18	
Combination chair/hole/pad	±0.34	
Back scale	±0.15	
Combination = bearing layer	±0.37	$1.5 * 0.37 = \pm 0.56$ mm
Bottom chair	±0.16	
Combination chair/hole/pad	±0.33	
Bottom scale	±0.18	
Combination = bearing layer	±0.48	$1.5 * 0.48 = \pm 0.72$ mm

be compensated for with an oversized polymer pad (250.5 ± 0.1 or 251.5 ± 0.1 mm) to maintain similar diameter tolerances. Imperfections in the hole geometry cause a different retaining action and extrusion of polyethylene with consequently larger vertical indentation.

(c) *Local contact pressure on an individual polymer bearing pad*

The maximum contact pressures for a single pad are calculated in Table 4 for the back and bottom bearing, based on (i) the calculations of global contact pressures over a full bearing area with $\Delta R = 10$ mm (Table 2), (ii) the effective distribution of pads, and (iii) the local deformation of pads implied by their tolerances. Local supports at the back of the concave surfaces cause a variation in stiffness and contribute to higher local contact pressures. Contact pressures on the front bearing are inferior and not critical. Applying stress intensity factors for different local effects, the design contact pressure for a single polymer pad is 150 MPa.

Compared to the original infinitely stiff MoS_2 layer, an elastic bearing interlayer causes a more homogeneous distribution of the contact stresses, and single polymer pads bear the local variations in stiffness or dimensional tolerances. Possibilities for redistribution of the contact stresses prevent the failure of the bearing layer over large areas. The material should have high bearing capacity to take up overloads, and high ductility for local plastic deformation (experimental verification). The levelling off of stress concentrations allows more accurate simulations and more representative test conditions for experimental verification tests.

The present redesign of the storm surge barrier is unique in its application of polymer pads under extremely high loads. Common contact stresses applied on UHMWPE are within 10–20 MPa, although there is no consensus regarding the true yield strength and design load ability of polyethylene. Collier et al. [10] cited a 21 MPa tensile yield strength for polyethylene while Buechel et al. [11] used a 32 MPa compressive yield strength and a damage threshold of 5 MPa. Bartel et al. [12] used a 12.7 MPa yield strength, while Hayes et al. [13] used 14 to 15 MPa. Bristol et al. [14] found that the contact stresses in several non-conforming designs are much larger than the tensile yield strength of the polymer, and rise towards 30 or 40 MPa with 80% of the total contact area that is typically overloaded above the damage threshold/fatigue strength.

4.3. Behaviour of machined steel structure

Normal and shear (friction) stresses are transmitted from the hybrid UHMWPE bearing element into the vertical walls and bottom plate of the machined holes through the visco-elastic deformation of the polymer. The strength of the underlying concave structure is detailed, and results in a maximum depth for the machined holes of 50 mm. The back concave structure is most critical in this respect, as supports beneath the surfaces locally reduce the thickness to 178 mm. No polymer pads are placed near those supports, avoiding overstress (Fig. 12). With a maximum depth of 50 mm and parallel to experiments on radial stiffness, the effective depth is $h_{\text{hole}} = 32$ mm.

Considering the polymer as a ‘liquid’ under yielding conditions or hydrostatic pressure, it is not able to transmit horizontal shear stresses. The carbon fibre/epoxy ring transmits the loads into the walls of the sample holder over an active height $h_{\text{eff,ring}} = 18.5$ mm in contact with the steel wall and width $b_{\text{ring}} = 20$ mm. The tensile and radial stress distributions in the ring were numerically evaluated [5]. They are used to estimate the steel capacity under a maximum contact pressure $p = 150$ MPa and coefficient of friction $\mu = 0.25$. As radial deformation is restricted under high loads, a machined hole can be considered as an equivalent pressure vessel with a pad diameter $D_{\text{pad}} = 250$ mm. The stresses acting on the steel are calculated as follows:

(a) *Stress-transfer under pure hydrostatic load at* $p = 150$ MPa

The average tensile force T in the carbon fibre/epoxy ring is calculated from Formula (1). The resultant horizontal force Q in the centre of the pad is calculated from Formula (2):

$$T = \frac{1}{2}(D_{\text{pad}} - 2b_{\text{ring}})h_{\text{eff,ring}}\,p \tag{1}$$

$$Q = p h_{\text{hole}} D_{\text{pad}} - 2T \tag{2}$$

resulting in $T = 291$ kN and $Q = 618$ kN. For an active load transmitting cross-section of the carbon/fibre epoxy ring $b_{\text{ring}} \times h_{\text{eff,ring}} = 370$ mm^2, the calculated average tensile

Table 4
Local contact pressures for a polymer pad in the back and front concave surfaces of the ball-joint

Design factor		Back bearing	Bottom bearing	Comments
Global contact pressure	MPa	31	34	Considering full bearing area
Loading factor	–	2.61	2.53	Depending on pad distribution
Factor difference in local stiffness	–	1.22	1.23	Non-uniform contact pressure distribution over bearing surface
Total contact pressure	MPa	99	106	
Local deformation	mm	2.70	2.80	Vertical indentation due to total contact pressure (experimental[a])
Extra deformation	mm	0.56	0.72	Imperfect geometrical tolerances on pad and hole
Additional contact pressure	MPa	48	57	Implied by deformation (experimental[a])
Total contact pressure (MPa)	MPa	147	163	Local working conditions for polymer pad

[a] Experimental values from stress–strain curve in Section 5.

stress σ_{YY} equals $T/(b_{\text{ring}} \times h_{\text{eff,ring}}) = 786$ MPa. This value corresponds to an effective simulated σ_{YY} under an overload $p = 163$ MPa. Assuming the polymer pad is under hydrostatic pressure and considering the steel wall as a pressure vessel is thus a good approximation.

(b) *Stress-transfer under maximum frictional load (shear stress)*

The horizontal friction force F transferred by the carbon fibre/epoxy ring with surface area A_{ring} is calculated from Formula (3). When added to the resultant horizontal force Q, it equals the total transmitted horizontal force on the steel wall H given by Formula (4). The momentum M on the steel wall is calculated from Formula (5).

$$F = \mu p A_{\text{ring}} = \mu p \pi (D_{\text{pad}} - b_{\text{ring}}) b_{\text{ring}} \tag{3}$$

$$H = Q + F \tag{4}$$

$$M = \frac{1}{2} Q h_{\text{hole}} + F \left(h_{\text{hole}} - \frac{h_{\text{eff,ring}}}{2} \right) \tag{5}$$

resulting in $F = 542$ kN, $H = 1160$ kN and $M = 22.22$ kN m. For a minimum wall thickness $t = 60$ mm, which follows from the distribution pattern of the bearing elements over the concave ball-joint surface, the maximum shear stress $\tau_{\max}$ and normal stresses $\sigma_{\max}$ are given by Formula (6) and Formula (7):

$$\tau_{\max} = \frac{3}{2} \frac{H}{D_{\text{pad}} t} \tag{6}$$

$$\sigma_{\max} = \frac{6M}{D_{\text{pad}} t^2} \tag{7}$$

resulting in $\tau_{\max} = 116$ MPa and $\sigma_{\max} = 148$ MPa as design values for maximum stresses in the steel wall. For a construction steel quality with yield strength 285 MPa, there is a safety-factor $f_{\text{normal}} = 285/148 = 1.93$ on yield failure by normal stresses and $f_{\text{shear}} = 285/(116\sqrt{3}) = 1.42$ on yield failure by shear in the smallest section. The present verification shows good local safety after redesign of the ball-joint while it considers that the highest contact pressures and highest coefficients of friction coincide on the same constrained bearing element, being rather conservative.

5. Experimental large-scale verification

The static strength, friction and wear behaviour of the polymer pads and convex counterfaces are large-scale tested for verification of their bearing capacity, stiffness and coefficients of friction. These values are determined under test conditions that agree with previous analysis, and they are further used as for the verification of the theoretical calculations. Only the principal results are given below, and we refer to Samyn et al. [15,16] for details on tests for different pad geometries. Every test was done three times, as more data increase the reliability of the test results, but have no improved significance for the real storm surge barrier. Statistical variation will be covered by introducing appropriate design factors.

5.1. Static loading

Hybrid UHMWPE pads (diameters 249.37 mm, 249.50 mm, 249.55 mm, thickness 40 mm) are loaded against a convex counterface between 0 and 150 MPa at 30 MPa/min in a vertical hydraulic press. Creep tests are done for a 24 h constant load at 30–150 MPa. In agreement with the climate conditions of the real construction, tests are done at 60% relative humidity and 23 °C environmental temperature. The test results are shown in Fig. 13(a) and (b) respectively. With the disc positioned into a circular holder, a maximum loading capacity of 400 MPa is guaranteed.

The stress–strain curves show that the initial point contact between the convex and the polymer pad causes local stress concentrations that are not dimensionally stabilised by the carbon fibre/epoxy ring due to the initial clearance between the bulk UHMWPE and its ring. Compared to the true stress–strain curves, this region corresponds to the elastic zone of the UHMWPE with a linear stress–strain relation. For higher strains, the central polymer element is fully constrained by its carbon fibre/epoxy ring and the walls of the machined hole. A non-linear relation is observed through the progressive indentation of the convex counterface below 50 MPa. At higher loads, the stiffness attains 3879 kN/mm at 120 MPa to 4910 kN/mm at 150 MPa (27% increase), corresponding to bulk modulus of 4200–5000 MPa with a Poisson coefficient $\nu = 0.473$–0.476. The stress–strain curves are more homogeneous for a second loading step, as the initial clearance does not have importance.

Creep deformation is limited to 0.15 mm at 150 MPa during the first loading step. After multiple loading steps, the deformation is similar for stepwise 90–150 MPa contact

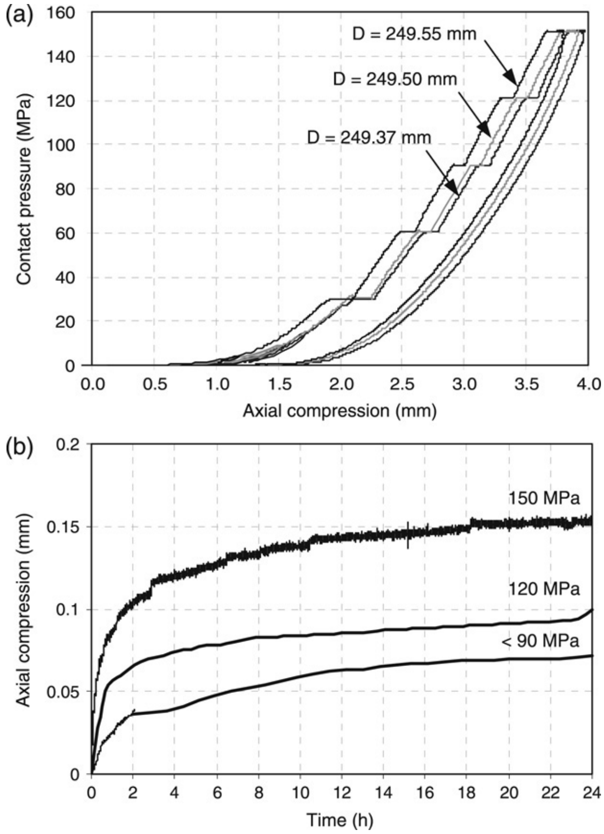

Fig. 13. Experimental static testing of the hybrid UHMWPE: (a) stress–strain curves for polymer pads with various diameter D into a machined hole with diameter 250 mm, (b) creep at different contact pressures.

pressures. This is an important issue with respect to the practical implementation and life-time use of the bearing elements in the ball-joint. Variable deformation is only concentrated within the first loading period at low loads. High initial deformation is observed at 30 MPa because visco-elastic deformation is initially attributed to elimination of the clearance; the creep is further controlled by total constraint after 45 min loading. At 75 MPa, the initial deformation step is somewhat reduced, because the immediate elastic deformation is larger and causes constraint by the sample holder: steady-state creep is then attained more frequently. After unloading and recovery (24 h), the permanent flow of surface diameter is 0.5% and permanent axial compression is 0.7%.

Avoiding contact between the scales and the chair structures, the polymer bearing surface should be at least 4 mm above the steel surface of the concave elements. Almost no wear of the UHMWPE surface is noticed during dynamic tests (Section 5.2) and only visco-elastic indentation or creep should be considered for the dimensional stability. It reveals from Fig. 13 that, depending on the effective pad diameter, the maximum indentation after 24 h creep at 150 MPa is 3.85 + 0.14 mm = 3.99 mm, with a remaining bearing layer thickness of 8 − 3.99 mm = 4.01 mm. The total vertical indentation after a life-time creep test (6 days) at 75 MPa is in the range of 1.69–1.99 mm, implying a bearing layer thickness between 6.0 and 6.3 mm.

5.2. Dynamic loading

Hybrid UHMWPE pads (Ø 175 mm × 40 mm) are reciprocally slid at 30–150 MPa against either steel St 37.2 N or a zinc–phosphate primer coating at 5 mm/s. In agreement with the climate conditions of the real construction, the tests are done at 60% relative humidity and 23 °C environmental temperature. The polymer surface temperature increases by frictional heating to a maximum of 65 °C bulk temperature and 120 °C flash temperature at 150 MPa. The static coefficient of friction μ_{s1} is measured at the start of the sliding motion,and the static coefficient friction μ_{sn} is measured at subsequent reversals of the sliding motion. The dynamic coefficient of friction μ_d is measured in the centre of the sliding stroke. Experimental values are summarised in Table 5.

Low friction is obtained under dry sliding conditions, without using external grease lubricants. A test with external grease lubricant does not show lower friction at 150 MPa because grease is squeezed out of the contact. The zinc–phosphate counterface beneficially lowers friction and shows good adhesion to the counterface without severe wear marks. However, the application method slightly influences the initial static coefficient of friction and dynamic coefficient of friction during the first sliding cycle: brushed coatings or sprayed and polished coatings provide lower static friction than rolled coatings. After several sliding cycles, the soft zinc–phosphate coating becomes smoothened, providing nearly identical friction conditions for the different application methods. Sprayed coatings with controllable thickness are finally preferred to protect the convex: the coating thickness ranges from 37 to 66 μm, with an average thickness of 51 μm after complete curing. Detrimental coating wear is observed after contact with the carbon fibre/epoxy ring and the coefficient of friction then increases to $\mu_{s1} = 0.11$ and $\mu_d = 0.07$ at 150 MPa.

The influence of three subsequent wear paths (100 m each, at 75 MPa) perpendicular to the motion of the friction test is experimentally investigated, revealing a gradual increase in static and dynamic coefficients of friction with ongoing sliding to $\mu_d = 0.16$ at 15 MPa and $\mu_d = 0.12$ at 30 MPa. Preliminary creep during 16 h at 50 MPa increases the initial static friction μ_{s1} from 0.10 to 0.21.

A modelling factor $\gamma_m = 1.25$ has been applied on the experimental coefficients of friction to compensate for statistical variations. The design coefficient of friction is determined from experimental results, considering the maximum friction after an intermediate wear path of 300 m and eventual creep:

- The global design criterion for friction does not assume that every pad is simultaneously subjected to maximum static friction, but the roll and slip motion of the ball-joint causes 80% of the pads to slide dynamically and 20% of the pads to break from the ball counterface and overcome static friction. The global design value of friction $\mu_{G;d}$ is estimated from Formula (8):

$$\mu_{G;d} = \gamma_m(0.80\mu_{d,\max} + 0.20\mu_{s1}) = 0.22. \tag{8}$$

Table 5
Experimental dynamic testing of hybrid UHMWPE polymer pads: Friction coefficients during sliding against bare steel and zinc–phosphate coating

p (MPa)	Steel counterface					Zinc–phosphate coating				
	Static			Dynamic		Static			Dynamic	
	μ_{s1}	$\mu_{s,\min}$	$\mu_{s,\max}$	$\mu_{d,\min}$	$\mu_{d,\max}$	μ_{s1}	$\mu_{s,\min}$	$\mu_{s,\max}$	$\mu_{d,\min}$	$\mu_{d,\max}$
15	0.12	0.11	0.12	0.10	0.11	0.10	0.11	0.12	0.08	0.09
30	0.10	0.10	0.11	0.09	0.10	0.10	0.08	0.09	0.07	0.08
60	0.08	0.07	0.08	0.06	0.07	0.05	0.06	0.07	0.04	0.04
90	0.06	0.05	0.06	0.05	0.05	0.04	0.05	0.05	0.03(5)	0.03(5)
120	0.05	0.05	0.05	0.04	0.04	0.03(5)	0.04	0.04	0.03	0.03
150	0.04	0.04	0.04	0.03(5)	0.03(5)	0.03	0.02(5)	0.03	0.02(5)	0.02(5)

- The local design coefficient of friction considers the maximum frictional force on one single hybrid UHMWPE-pad during the first sliding pass (Formula (9)) and subsequent sliding passes (Formula (10)).

$$\mu_{L;s1,d} = \gamma_m \mu_{s1} = 0.26 \quad (9)$$

$$\mu_{L;sn,d} = \gamma_m \mu_{sn} = 0.21. \quad (10)$$

Coefficients of friction used for design of the ball-joint reveal that global values are below the design limit of $\mu_{G;d} < 0.25$ (Section 4.1). The present solution fits the strength requirements implied by the steel structure. The contact between a UHMWPE pad/zinc–phosphate coating has a considerably long running-in period with high initial static friction. It was calculated that the contact stresses on the back, front and bottom chairs during floating are lower than at steady-state contact and higher coefficients of friction are tolerated.

6. Failure analysis

The reliability of the storm surge barrier is defined by three failure modes: not closing ($P_{\text{nc,total}} = 10^{-3}$ per operation), not opening ($P_{\text{no,total}} = 10^{-4}$ per operation) and collapse ($P_{\text{c,toal}} = 10^{-6}$ per year). From a full probabilistic approach, the critical loads and effects of an overload combination are determined for every element in the structure. Overloads are related to the various failure modes (principles explained by, e.g., Vrijling [17]). The failure probabilities for every structural element are determined according to NEN 6770, NEN 6771 and NEN 6772, but the original probability of $1.6 \cdot 10^{-4}$ per life-time and per component with a 50 year life-time was changed into the level required for the storm surge barrier, i.e. the original reliability factor $\beta_{\text{norm}} = 3.6$ becomes $\beta = 4.3$ and a 100 year life-time is assumed. It is concluded that the collapse event is the most important failure mode for every loading history of floating, immersion, retaining or reverse operations. The probability for collapse is $P_{f,\text{joint}} = 5 \cdot 10^{-8}$ per year for one single ball-joint.

6.1. Influences of the closing frequency

Compared to the original design, the operating frequency of the storm surge barrier has increased due to the lowering of the critical storm level from 3.20 to 2.80 m + NAP (Amsterdam Ordnance Datum) and performing test operations once a year. It is concluded, however, that the failure probability is not significantly influenced by a more frequent use of the construction. Annual test operations do not use the full strength range of the construction, because the hydraulic loads are lower compared to a full retaining operation. The available information for failure models improves through more frequent use of the barrier, and the failure procedures can be calculated more accurately with a small decrease in failure probability.

6.2. Strength and load of the modified ball-joint

Collapse of the ball-joint is defined as the failure in one or more constructional elements when the load carrying capacity of the joint is exceeded. The constructional safety is verified according to the “design point” analysis in Formula (11), expressing the failure probability P_f as an exceedance level of the load S and strength R.

$$S_d \leq R_d \quad \text{or} \quad S_k \cdot \gamma_s \leq R_k/\gamma_r \quad (11)$$

with the design load S_d, the design strength R_d, a characteristic load S_k (95% fractile of the real load distribution), a characteristic strength R_k and partial safety factors γ_s for loads and γ_r for strength. The strength is verified for linear-elastic material characteristics, not taking into account eventual reserves against failure through plastic deformation.

Verification is done for three loading histories on the retaining wall, characteristic for loading the front, back and bottom bearing elements of the ball-joint. The maximum design coefficient of friction $\mu = 0.25$ and the effective stiffness of the bearing interlayer are applied, as experimentally determined. Additionally to the original design, a loading history during floating is verified with a maximum coefficient of friction $\mu = 0.50$, representing eventual contact between concave and convex surfaces for the lower ΔR. The strength safety factors for every component in the modified ball-joint structure are calculated in Table 6, and they agree with the original design values. Calculations show a failure probability for the design load of P_f $(S > S_d) = 2.8 \cdot 10^{-4}$ per lifetime (or $4.0 \cdot 10^{-6}$ per year), and a failure probability for the design strength of $P_f(R < R_d) = 5.0 \cdot 10^{-4}$ per lifetime (or $6.6 \cdot 10^{-6}$ per year). The strength capacity of the modified structure is approved.

7. Manufacturing and installation

The holes in the concave structures are manufactured as shown in Fig. 14(a) and the hybrid UHMWPE pads are

Table 6
Partial safety factors and global loading capacities of different structural components in the ball-joint

Component	Safety factor γ_r	Yield strength (MPa)	Loading capacity R (MPa)
Connection between steel trusses and ball-joint kernel	1.38	Thickness < 200 mm: $\sigma_y = 355$ Thickness = 200 mm: $\sigma_y = 335$	257 257
Convex surfaces	1.34	$\sigma_y = 285$	213 (linear stresses) 285 (peak stresses)
Concave surfaces	1.46	$\sigma_y = 285$	195 (linear stresses) 285 (peak stresses)
Welds	1.35	$\sigma_y = 510$	377
Bolts	1.35	$\sigma_y = 510$	377

(a) (b)

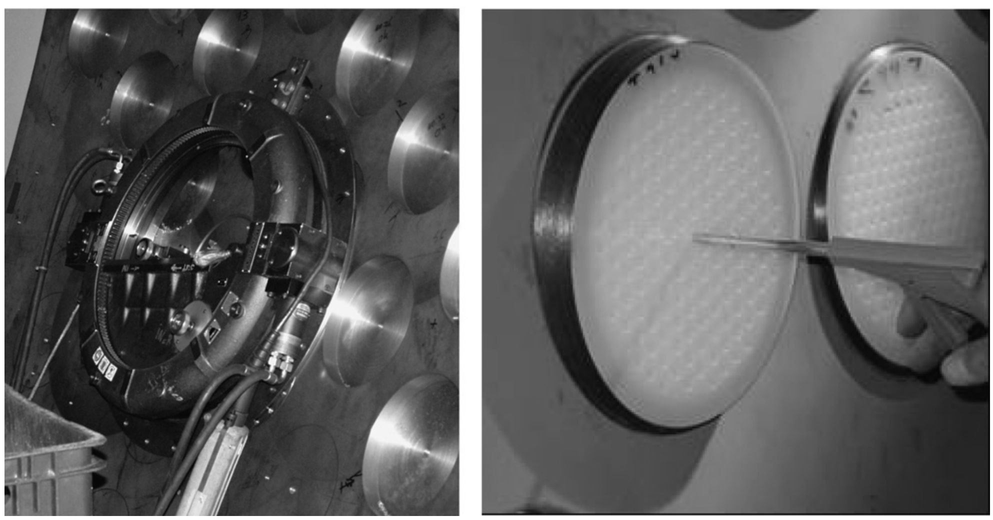

Fig. 14. Manufacturing and installation, (a) machining of the holes, (b) positioning of the hybrid UHMWPE pads.

mounted as shown in Fig. 14(b). All modifications on the back and front chairs are performed on-site, within a small space (300 mm) between the convex and concave structures. For the modification of the bottom chair structure, the ball-joint kernel was lifted over 550 mm. A special tool for machining the holes was developed, which is positioned at the centre point of every hole to be made. The tolerance of the hole diameters is in agreement with traditional machining operations. The pads are mounted with easy hand force while axial fixation is guaranteed by the rubber O-ring. The roughness of the bottom and the side walls of the machined holes possibly influences the deformation and creep behaviour of a retained polymer disc. Therefore, it should be controlled at $Ra = 3.2$ µm, as simulated in present full-scale tests.

In-the-field test operations of the storm surge barrier in September 2004 and September 2005 demonstrated its reliable functioning. The deformation of the hybrid UHMWPE pads corresponds exactly to the phenomena observed during the full-scale laboratory tests. During functioning, the eventual up-lift of the pads is avoided through the small space (30 mm) between the convex and concave surfaces. In case of damage, the pads can be easily replaced. They are removed from the retaining holes by air pressure through a central hole in the hybrid UHMWPE pad. According to previous calculations and in-the-field observations, the total life-time of the structure is presently estimated at 100 years.

8. Conclusions

The ball-joint construction is a critical point in the functionality of the present storm surge barrier. For a maximum transmitted bearing load of $350 \cdot 10^6$ N, the sliding surfaces of the joint were initially covered with a thin lubricating film. The film provides low friction, but failure of the film causes delamination and cold-welding. Analysis shows that standard small-scale laboratory tests were not able to simulate the working conditions of the sliding components. A global analysis of the construction under different loading histories is presented in this paper in order to determine and verify reliable large-scale tests.

The reliability of the storm surge barrier is improved by the incorporation of an elastic bearing layer consisting of ultra high molecular weight polyethylene (UHMWPE) pads reinforced by a carbon fibre ring. By lowering the elasticity, increasing the coefficient of friction, and increasing thickness of the bearing layer, the bearing force becomes higher. Through the combined rolling/slip behaviour of the convex surface into the concave supports, the bearing force attains extreme positions more frequently and the loads on the construction increase. Additional rotations occur due to the deflection of the steel trusses under the action of wind and hydraulic loads.

For different loading histories including floating, immersion and retaining of the barrier, the ball-joint is loaded from the initial gravity weight to a full hydraulic head. Loads on the ball-joint are most critical when gravity forces are lowest and the hydraulic forces perpendicular to the gates are highest. For a bearing layer thickness of 10 mm, the maximum design coefficient of friction is 0.25 and may increase to 0.50 during running-in.

The stiffness, dimensional stability and coefficient of friction are verified by large-scale experiments on the polymer pads. The local design contact pressure per pad is calculated from an optimum distribution factor and attains 150 MPa. The tolerances on the bearing surfaces and the polymer pads are important factors in determining the stiffness and deformation of the bearing layer. Large-scale experiments are in agreement with an on-site closing operation of the storm surge barrier.

Acknowledgements

The authors express their gratitude to the Ministry of Transport, Public Works and Water Management (The Netherlands) and Solico B.V., allowing us to present the test results and to be involved in the redesign of the Maeslant storm surge barrier.

References

[1] Gerritsen H. What happened in 1953? — The big flood in The Netherlands in retrospect. Phil Trans Roy Soc A — Math Phys Eng Sci 2005;363: 1271–91.

[2] Van Dantzig D, Kriens J. The economic decision problem of safeguarding the Netherlands against floods. Report of the Delta Committee. The Hague.

[3] Vollebregt EAH, Roest MRT, Lander JWM. Large scale computing at Rijkswaterstaat. Parallel Comput 2003;29:1–20.

[4] De Jong MPC, Battjes JA. Seiche characteristics of Rotterdam Harbour. Coastal Eng 2004;51:373–86.

[5] Van Schepdael L, Leendertz JS, Van Paepegem W, Samyn P, De Baets P, Degrieck J. Carbon fibre reinforced pad design for the modification of the ball bearing of the storm surge barrier near Rotterdam. Mater Struct 2006 [in press].

[6] Vanoorschot JH, Pruijssers AF. Storm-surge barrier in the new waterway. Proc Inst Civil Eng — Water Maritime Energy 1995;112:159–67.

[7] Zondervan A. The storm surge barrier in the 'Nieuwe Waterweg' near Rotterdam, Netherlands. Fabrication and assembling of the tubular structures. Technical report Hollandia B.V, Krimpen a/d Ijssel; 1997.

[8] Van de Velde F, De Baets P. The friction and wear behaviour of polyamide 6 sliding against steel at low velocity under very high contact pressure. Wear 1997;209:106–14.

[9] Blanchet TA, Kennedy FE. Effects of oscillatory speed and mutual overlap on the tribological behaviour of PTFE and selected PTFE-based self-lubricating materials. Tribol Trans 1991;34:327–34.

[10] Collier JP, Mayor MB, McNamara JL. Analysis of the failure of 122 polyethylene inserts from uncemented tibial knee components. Clin Orthop Relat Res 1991;273:232–42.

[11] Buechel FF, Pappas MJ, Makris G. Evaluation of contact stress in metal-backed patellar replacements. Clin Orthop Rel Res 1991;273:190–7.

[12] Bartel DL, Bicknell VL, Wright TM. The effect of conformity, thickness and material stresses in UHMWPE components for total joint replacement. J Bone Joint Surg 1986;68A:1041–51.

[13] Hayes WC, Lathi VK, Takeuchi TY. Patello-femoral contact pressures exceed the compressive yield strength of UHMWPE in total knee replacements. In: Transactions of 39th ORS; 1993. p. 421.

[14] Bristol RE, Fitzpatrick DC, Brown TD, Callaghan JJ. Non-uniformity of contact stress on polyethylene inserts in total knee athroplasty. Clin Biomech 1996;11(2):75–80.

[15] Samyn P, Van Schepdael L, Leendertz JS, Van Paepegem W, De Baets P, Degrieck J. Deformation of reinforced polymer bearing elements on full-scale compressive strength and creep tests under yielding conditions. Polym Test 2006;25(2):230–45.

[16] Samyn P, Van Schepdael L, Leendertz JS, Gerber A, Van Paepegem W, De Baets P, et al. Large-scale friction and wear tests on a hybrid UHMWPE-pad/Primer Coating combination used as bearing element in an extremely high-loaded ball-joint. Tribol Internat 2006;39(8):796–811.

[17] Vrijling JK. Probabilistic design of water defense systems in The Netherlands. Reliab Eng Syst Safe 2001;74:337–44.